RSC Advances

ROYAL SOCIETY OF CHEMISTRY

www.rsc.org/advances

Dynamics of roughening and growth kinetics of CdS-polyaniline thin films synthesized by Langmuir-Blodgett technique

Nayan M. Das[a]*, *Dhrubojyoti Roy*[a], *Nigel Clarke*[b], *V. Ganesan*[c], *Partha S. Gupta*[a]

[a]Nanoscience and Thin Film Laboratory, Department of Applied Physics, Indian School of Mines, Dhanbad-826004, India

[b]Department of Physics and Astronomy, University of Sheffield, Hicks Building, Hounsfield Road, Sheffield S3 7RH, United Kingdom

[c]UGC-DAE Consortium for Scientific Research, University Campus, Khandwa Road, Indore-452017, India

***Corresponding Author:** nayanmanidas3@gmail.com; Telephone: +91 8987520079; Fax: +91-3262296563;

Abstract:

Thin films of cadmium sulphide (CdS) nanoparticle induced polyaniline (PANI) nanocomposites have worked as a better system for the application in photovoltaics due to the efficient charge separation and charge transfer. In this communication, we have chosen such a system of varying thickness deposited by Langmuir-Blodgett (LB) technique in order to study the growth and roughness phenomena by dynamic scaling theory. Different techniques such as X-ray photoelectron spectroscopy (XPS), atomic force microscopy (AFM) and X-ray reflectivity (XRR) are used for characterization of these films. In the study, the growth exponent, β is found to have a correlation with invariant logarithmic scaling law. A very large value of $\beta = 1.18 \pm 0.23$ as calculated is a result of the rapid roughening in the multilayer film growth process. We have investigated the dynamic scaling behavior of multilayer system which shows a difference in the value of the coarsening factor and this confirms the breakdown of self-affinity as a consequence of some nonlocal growth effects. The normal grain formation with deposition at initial stage and the increase in grain abnormality with increase in thickness is also verified in support of the dynamic scaling ansatz. In the present study the layer-by layer deposition is confirmed by XRR fitting for a 3 layer film whereas the multilayer shows diffusing behavior due to H-bonding or electrostatic interactions.

Keywords: Langmuir-Blodgett multilayer films; CdS-Polyaniline nanocomposites, atomic force microscopy, dynamic scaling factor, X-ray reflectivity.

Introduction:

Multilayer composites of semiconducting nanoparticles and conducting polymers provide large contributions in the field of photovoltaics, heterogeneous catalysis, sensors, actuators etc. [1-6]. In order to prepare a thin film of composite material for practical applications, we need a better understanding of the mechanism of their self-assembly at the molecular level. Optimized results for polymer composite devices can be achieved when molecular control over multilayer deposition is gained. However, this requires precise knowledge of the physics and chemistry of such materials [7,8]. The improvement in properties by controlling the aggregation of semiconducting nanoparticles in polymer is a challenge as the nanoparticles are highly unstable in the polymer matrices. Research has been carried out by using the surfactant and other shielding agents to incorporate such nano-entities within the polymer chains. Although the approach for nanoparticle dispersion in polymer is successful in some cases [2-5, 9], in the present work we have found that the particles can exhibit self-assembly into some agglomerated structures. Reports confirming such aggregated dispersions show beneficial effects on the mechanical properties of the resulting nanocomposites [10].

Polyaniline (PANI) is regarded as one of the most promising organic compounds due to its conductivity in the emeraldine salt (ES) form and also for the ease in the process of its synthesis [11]. In the emaraldine base (EB) form this polymer is chemically doped with different acids like hydrochloric acid (HCl), camphorsulphonic acid (CSA), dodecylbenzenesulphonic acid (DBSA) etc. to convert to ES form [12-14]. The characteristic tunability of electrical and optical properties as well as the higher stability of PANI make them highly suitable for organic electronic devices. The properties of PANI are further enhanced by the change in the oxidation states or by blending with other nanosized semiconducting materials [15]. In this respect, cadmium sulphide (CdS) incorporated PANI nanocomposites have been used in photovoltaic applications due to the formation of large internal area which can facilitate efficient charge transfer [15,16]. Devices made out of such nanocomposites exhibit reduced light scattering effects and charges generated are easily transported by the respective carrier to the specific electrodes [17]. It has been reported that the enhanced charge transfer is only possible if the charge carrying species find the easy paths for the electrode to carry the charges. Thickness variation of the composite may better serve

in this respect by making vertical chain attachment of the charge carrying species [18]. Although the results by varying the thickness have shown enhanced conductivity with better charge separation, the production of better thin films with uniform thickness and lesser roughness remains a topic of research. This motivates the present work to investigate the changes in the surface properties in CdS incorporated PANI-CSA thin films with variation of thickness.

Again, fabrication of ultra thin films of nanocomposites shows little absorption of X-rays, light photons etc. in the molecular level due to small thickness. Better surfaces in the mesoscopic level may remove the above difficulties. The variation in structural and morphological properties of the multilayer films can be studied as a shift of thickness from the nano-region to the mesoscopic stage [19-21]. The layer-by-layer fabrication leads to specific top surfaces with variation in interfacial roughness. Most of the rough surfaces exhibit significant self-affine properties upto a certain range of length scale. The top surface shows the growth in fractals where the use of the scaling behavior and fractal dimension calculation provides the extent of self-affinity of the films [22]. In this level the nature of the composite thin films can be studied by the dynamic scaling theory (DST). The growth exponent and the roughness exponent are studied in order to understand the surface behavior with layer variation [23]. Statistical evaluation of the surface structure by means of the power spectral density (PSD) technique is also favorable for study of the lateral and transverse growth of the thin films [24].

The growth of the films by the thickness variation is a scale invariant phenomenon [25]. Hence the growth is ruled by some macroscopic power laws without any specific scales. In case of self-affine surfaces, the variation of RMS roughness with time t and the length l follow the Family-Vicsek scaling [25],

$$\sigma(l,t) \sim t^{\beta} F(lt^{-1/z}) \sim \begin{cases} l^{\alpha} \; for, l \ll l^{*} \\ l^{\beta} \; for, l \gg l^{*} \end{cases} \quad (1)$$

Where F is a scaling function, α and β are roughness and growth exponents respectively, the dynamic scaling factor is measured as, $z = \alpha/\beta$ upto a crossover length scale $l^{*} \sim t^{1/z}$.

In a growth process where the film thickness h, is proportional to the time of deposition t, then within the asymptotical limits, the roughness (σ) variation is given as [23, 26],

$$\sigma(h) = ah^{\beta} \quad (2)$$

where a is proportionality constant.

The RMS roughness is a scale invariant parameter and for n×n discretized image points over the film surfaces, it gives a single value [24]. Therefore there is every possibility of having the same roughness values for the surfaces of very different morphology and different behaviors. To avoid this, the PSD calculations are also carried out here which consider the roughness calculation at each length scale. Such a calculation is more reliable as the measurements include very large and very small height fluctuations [24]. Furthermore, the grain growth phenomenon and the agglomeration over the surface of the films with the layer variation are also considered for the structural morphology study of the films. The overall detail of the surface and interface structure as the variation of film thickness is discussed in the article.

2. Experimental Procedure:

2.1. Chemicals and Materials: Polyaniline (99%) (PANI, Sigma Aldrich) in the emeraldine salt form is dissolved in ammonia solution (pro analysi, 25%GR, Merck) overnight and is filtered to obtain in base form. Camphorsulphonic acid (SRL, India) and m-cresol (Merck) are used as received. Analytical grade chloroform ($CHCl_3$, 1–2% v/v ethanol as preservative) is used as a spreading solvent for the composite material. Methanol is used as a solvent for cadmium chloride ($CdCl_2.H_2O$, Merck) and sodium sulphide ($Na_2S.xH_2O$, Rankem). Ultra-purified Milli-Q (Merck, Millipore) water having a resistivity of 18.2 MΩ.m is used as the subphase over the LB trough. All the above materials except polyaniline are used as received. Polyaniline in the base form is obtained as a residue after the filtration and the same is dried in a closed vessel.

2.2. Preparation of PANI–CSA and CdS incorporated PANI–CSA solution: For the preparation of the thin films, initially 1mg/mL of PANI is dissolved in a solution containing 90% of chloroform and 10% of m-cresol v/v. The prepared solution is sonicated in an ultrasonic bath sonicator for 2 hours. The color of the whole solution turns to blue with some undissolved residue. CSA with an amount of 4 times that of PANI is added to the above solution and again the mixed solution is stirred in a magnetic stirrer until whole of the solution appears to be green. The change in the color confirms the protonation of PANI with acid. The solution is filtered with watman-2 filter paper to get rid of the undissolved macromolecules. Two separate solutions of 2 mM concentration of $CdCl_2$ and Na_2S are prepared using 10 mL of methanol as solvent in each. The prepared solutions are ultrasonicated for 1 hour. After sonication both the solution in methanol appeared to be transparent. Now, in order to make the CdS incorporated PANI-CSA nanocomposite,

carefully 10 drops (~2ml) of each of $CdCl_2$ solution and Na_2S solution are mixed with PANI containing solution.

A probable scheme for the formation of the CdS incorporated PANI-CSA nanocomposited is shown in Figure 1.

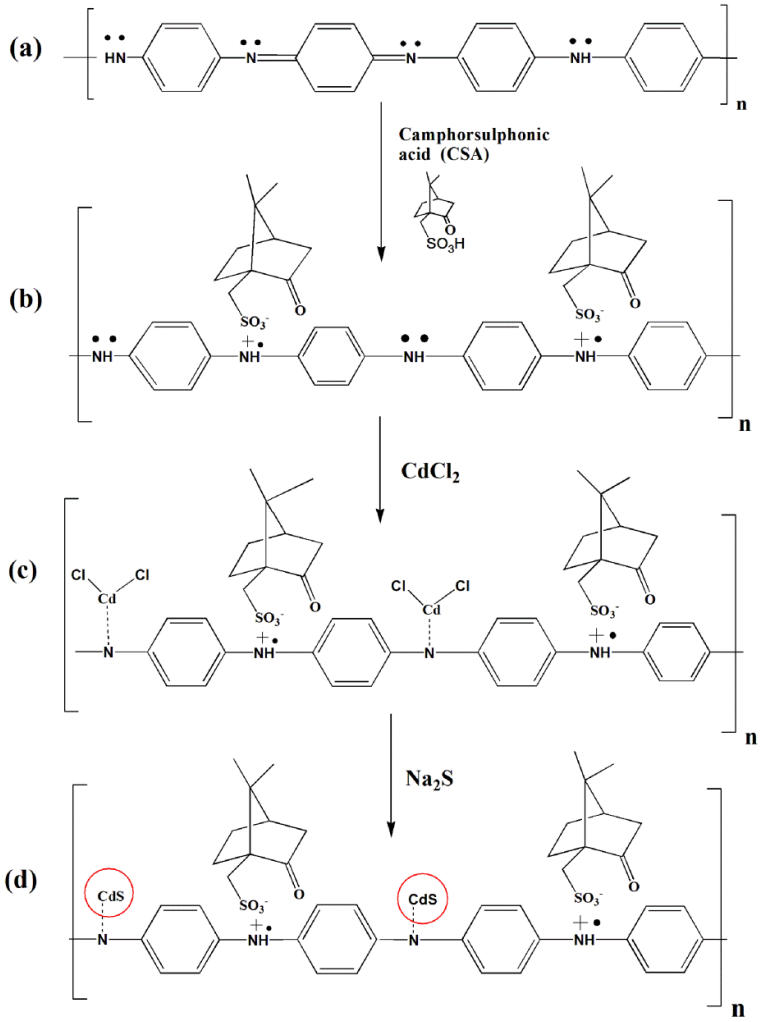

Figure 1: A scheme showing the CdS incorporation with PANI-CSA to form the nanocomposite.

2.3. LB film deposition: A Langmuir-Blodgett (LB) unit (Apex Instruments Co. India) is used to fabricate the thin layers of CdS incorporated PANI-CSA over the glass substrate. The LB trough and the substrates are cleaned as discussed in our earlier publication [8]. The trough is filled with the ultra purified deionized water which is used as the subphase. The pH of the solution is made acidic and maintained at a value of 2.5–2.8 by adding HCl to the water subphase. After cleaning the subphase surface, separate monolayer of each of PANI-CSA

solution and CdS incorporated PANI-CSA composite solution are spread over it by a micro-liter syringe (Hamilton make). The volume spread in each case is maintained to be 800 µl. Since chloroform is highly evaporating, the monolayer films are left undisturbed over the water subphase for a period of 20 minutes to get rid of the solvent molecules. After complete evaporation of the solvent molecules the film molecules are left in the gaseous phase. The isotherms are checked for both neat PANI–CSA and CdS incorporated PANI–CSA solution separately in order to investigate any phase change during compression. The CdS incorporated PANI–CSA thin films are deposited on the glass substrate at surface pressure of 12 mN/m. All the depositions are carried out at the room temperature. The compression speed of the barrier over the trough is controlled to be at 20 mm/min. Such a high compression speed is optimized after several performances for better stability for multilayer deposition by maintaining the transfer ratio value around unity. The dipping and the lifting speed are also fixed at a speed of 3 mm/min. 30 minutes of elapsing time between the first and the second layer is adjusted and from the next deposition onwards, the substrates are kept at 8 min in air and 5 min inside the water subphase for drying. LB films of 3 layers, 9 layers, 15 layers, 19 layers, 21 layers and 25 layers are fabricated over glass substrate for the current investigation.

2.4. Analyses:

2.4.1. AFM image analysis: AFM (Digital Instruments Nanoscope-IV, with Si_3N_4 100µm. cantilever, 0.58 N/m force constant) is used to measure the average height and the structural details of the films in contact mode. We used standard silicon nitride (Si_3N_4) pyramidal tips mounted on triangular cantilevers. Scan areas are varied from 2×2 μm^2 to 10×10 μm^2 over several portion of film surface in order to get the reliable image pictures. Sharp needle-like tip is used so as to minimize the tip induced modification of in the LB films. The scan rate is kept constant at a resonance frequency of 300 kHz to obtain stable images. The images so obtained are flattened by using a simple polynomial function to remove the curvature that results from the movement of the tube piezoelectric scanner. Windows Scanning x Microscope (WSxM) software [27] is used for image processing and analysis.

2.4.2. TEM analysis: TEM (FEI-Tecnai-G20 with a LaB6 filament, operated at 200 keV) was used to study the size and structural properties of nanoparticles.

2.4.3. XPS analyses: For element analysis of the LB films, XPS measurements are performed with Omnicron Multiprobe spectrometer fitted with an EA 125 hemispherical analyzer and a monochromatized Al-Kα (1486.6 eV) source. All data are collected at pass energy of 40 eV with analyzer angular acceptance at ±1°.

2.4.4. XRR analysis: The thickness of the thin film and the electron density profiles are calculated by the XRR measurements using the high resolution X-ray diffraction system (Bruker D8 Discover Diffractometer using Cu-K_α, λ=1.543 Å wavelength). The reflectivity measurements are carried out up to the incident angle of 4° and are analysed by the parratt32 software. The layer-by-layer variation of the electron density and the interfacial roughness are considered for the fitting of the reflectivity spectra. Individual layer height, electron density and interfacial roughness are evaluated in layer-by-layer format.

2.4.5. FTIR analyses: The Fourier transform infrared (FTIR) spectra are recorded in the wavenumber range 2000–400 cm^{-1} using a Perkin-Elmer make FTIR-2000 spectrometer.

2.4.6. UV-Visible analysis: The UV-Visible-NIR measurements are carried out by using Carry series UV-Vis-NIR spectrophotometer (Agilent Technologies).

3. Results and discussions

3.1. *Pressure–area (π–A) isotherm:*

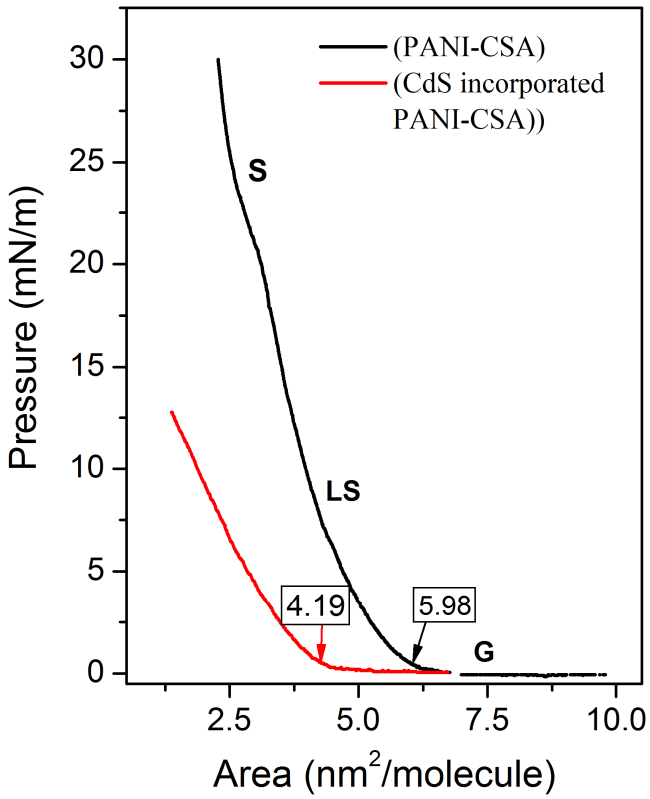

Figure 2: The pressure vs. area per molecule (π-A) isotherm of PANI–CSA (black solid line) and CdS incorporated PANI–CSA (red solid line) monolayer over water subphase.

The π–A isotherm curves of PANI–CSA and CdS incorporated PANI–CSA monolayer over water subphase at the room temperature are shown in Figure 2. The deposition of PANI–CSA thin films over glass substrate is done at a surface pressure of 30 mN/m (black line, Figure 2). The isotherm curve in case of PANI–CSA displays the area distribution which passes through gaseous (G), liquid-solid (LS), solid (S) phases while compressing the monolayer over subphase. On the other hand the isotherm for CdS doped PANI–CSA monolayer shows a monophasic rise [after (G) gaseous phase] upto the surface pressure of 12 mN/m (red graph, in Figure 2). The change in the area per molecule (a_m) for the isotherm is given by,

$$a_m = \frac{A M_w}{c N_A V} \quad (3)$$

Where A is the area of the water surface enclosed by the trough barriers, M_w the molecular weight, c is the concentration of the spreading solution, N_A is the Avogadro's number, and V is the volume of the solution spread over the water surface.

From the isotherm curves limiting pressures of PANI–CSA and CdS–PANI–CSA have been calculated to be 5.98 nm^2/molecule and 4.19 nm^2/molecule respectively. The limiting surface area values can be evaluated from the steeply rise in the isotherm curves with respect to the zero pressure values. The difference in the limiting areas may be because of the segmental repulsion which is prominent amongst the different components of the PANI–CSA and CdS incorporated PANI–CSA. The larger limiting area in neat PANI-CSA is because of the charged segments of the partially positively charged polymer chains, since the smaller unit of CSA cannot compensate the charges of polymer. This leads to the segmental repulsion amongst its constituents. High level of segmental repulsion will lead to the more extended conformation of the surfaces. On the other hand the incorporation of negatively charged CdS nanoparticles in PANI–CSA system decreases the segmental repulsion by charge compensation in between the different segments. Thus an increased interaction amongst the different constituents results in more compact spreading. From Figure 2, one can also conclude that the low value of saturation surface pressure in CdS incorporated PANI–CSA system reduces amphiphilic property of the system along with decrease in stability.

3.2. Structural morphology study

3.2.1. TEM study:

The structural morphology of the CdS nanoparticles formed within the nanocomposites is studied using the high resolution transmission electron microscope (HRTEM) as shown in

Figure 3(a-d). It is seen from Figure 3(a) that the polymer nanocomposite contains a large number of CdS nanoparticles. The sizes of the nanoparticles as calculated from the high resolution images are found to be varying in the range of 6-9 nm (Figure 3(c)). The d-spacing value is also calculated to be 3.24 Å from the lattice fringes of the CdS nanoparticles. From Figure 3(d) it is confirmed that the growth of nanocomposite follows nucleation of CdS nanoparticles within PANI-CSA polymer matrix.

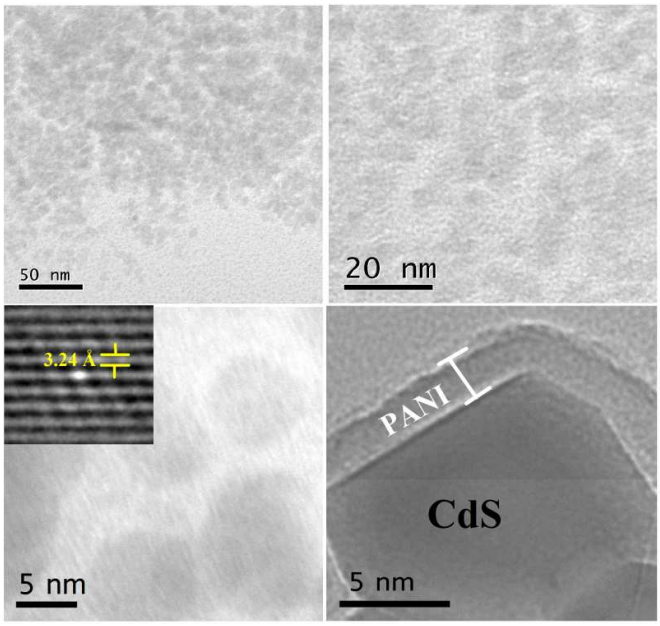

Figure 3: (a)-(c) TEM images of CdS within the polymer matrix at various scale resolutions. The calculated d-spacing of CdS nanoparticle lattice fringes are shown as inset in image(c); (d) nucleated growth of CdS in polymer is shown.

3.2.2 XPS study:

The presence of different atomic constituents of the film materials have been confirmed by the XPS measurements. The spectra in the Figure 4 show the presence of C, O, N, Cd and S in their relative percentage compositions. The C 1s peaks are spanning over ~283 eV to 290 eV and the spectra is deconvoluted in three individual peaks. The peak at around 283.91 eV represents the C of benzenoid ring with contributions from protonated imine and amine sites; second peak at 284.71 eV represents origin of the neutral C-C/C-H bond of PANI backbone and the last convoluted peak at around 285.86 eV represents $C\text{-}N^{+}/C{=}N^{+}$ bonding and the C=O/C-O bonding [28]. The O 1s, centered at 533.75 eV is convoluted to two peaks at around 532.78 eV and 534.39 eV respectively suggesting the peak due to acid group and the presence of oxygen impurities during the synthesis of films [29].

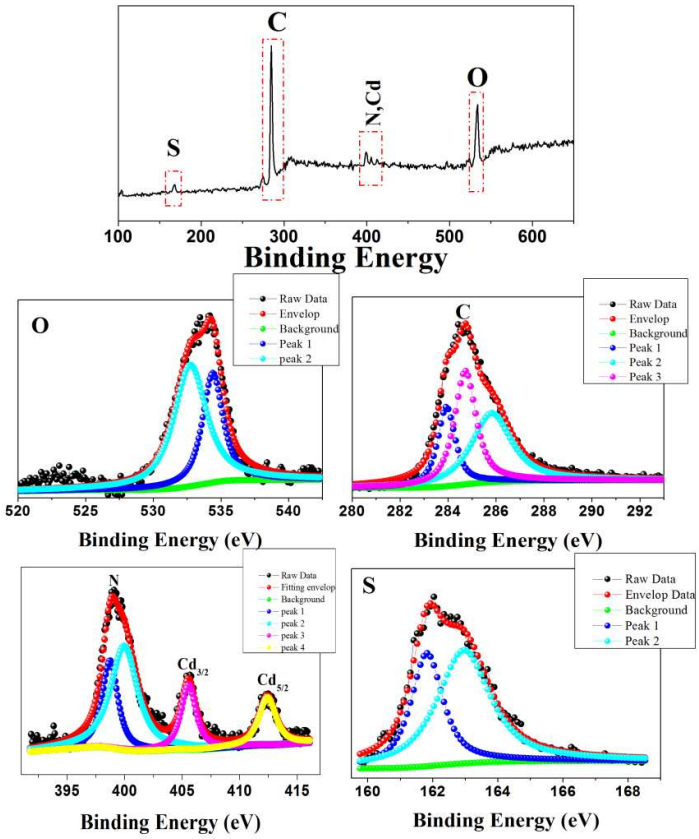

Figure 4: XPS spectra showing the presence of CdS in polymer nanocomposite LB films.

From the XPS spectra it is seen that the binding energy values for cadmium (Cd) and nitrogen (N) peaks are very closely placed. N peak is seen at around 399.28 eV and is resolved into two peaks at 398.72 eV and 399.9 eV confirming the attribution of nitrogen from benzenoid di-amine and quinoid di-imine of PANI respectively [30]. The peaks of cadmium atoms at ~405.55 eV and 412.21 eV correspond to Cd $3d_{3/2}$ and Cd $3d_{5/2}$ states respectively [31]. The presence of S peak is found to be at ~162.03 eV which when resolved shows two distinct positions at 161.83 eV and 162.96 eV respectively suggesting the presence of S $2p_{3/2}$ state.

3.3. Optical study

3.3.1. FTIR study of PANI-CSA and CdS incorporated PANI-CSA

The FTIR spectrum of the PANI-CSA and CdS incorporated PANI-CSA in the range 400–2000 cm^{-1} is shown in Figure 5. The different vibration spectra show the presence of different bands in PANI-CSA and CdS incorporated PANI-CSA composites. The higher frequency vibration at ~1578 cm^{-1} is due to the major contribution from the quinoid rings while the

lower frequency mode at ~1457 cm^{-1} proves the presence of benzenoid ring units of the polymer. The shifting of peaks due to the formation of CdS incorporated PANI-CSA composite with respect to the neat PANI-CSA is tabulated in the table 1. The formation of the composite is also confirmed further by the UV-Visible spectra.

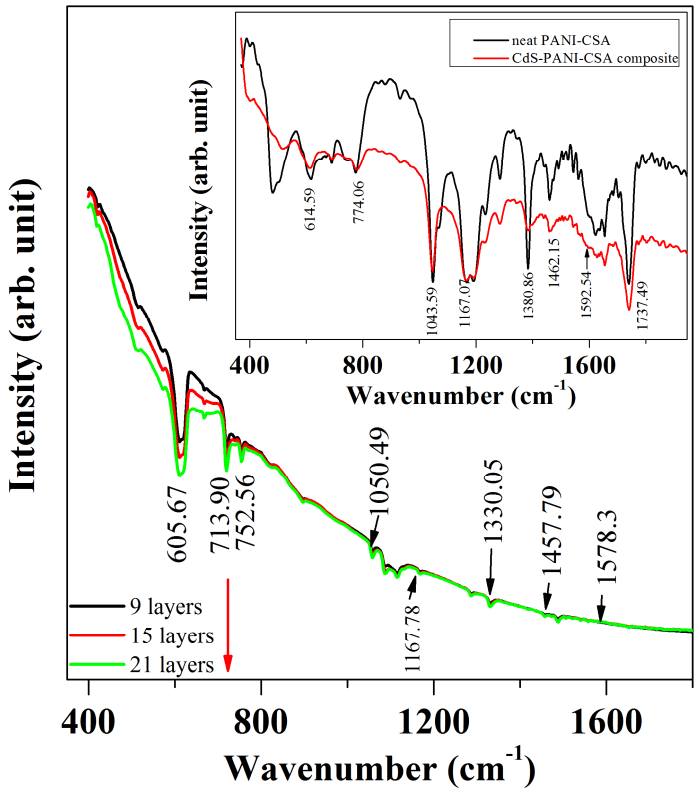

Figure 5: FTIR spectra of neat PANI-CSA and CdS incorporated PANI-CSA thin film are shown. In the inset the corresponding FTIR spectra of the solution are shown.

3.3.2. UV-Visible absorption study

The UV–Visible absorption spectra of PANI–CSA and CdS incorporated PANI–CSA nano-composite thin films are shown in Figure 6 and the corresponding absorption spectra of the respective solutions are shown in the inset of Figure 6. From the figure three characteristic absorption bands of PANI–CSA are seen at positions 300 nm, 426 nm and 800 nm [35]. Out of the different absorption bands, the band at ~300 nm is attributed to the π-π* transition of the benzenoid ring. The second band at 426 nm is assigned polaron–π* transition. This specific band confirms the protonated form of the acid doped polyaniline. The band at 800 nm, which is responsible for the green colour of the polymer, is due to trapped exitons

located on the quinoid imine moieties. This band is a broad one and corresponds to π–polaron transition which is related to the formation of localized polarons at the backbone of polymer [36]. On the otherhand the corresponding absorption bands of the CdS incorporated PANI-CSA are found to be red shifted. The new band positions of the nanocomposite are listed to be at about 308 nm, 440 nm and 843 nm respectively. The observed red shift in the absorption bands is be due to the incorporation of CdS nanoparticles and their interaction with PANI [37]. From the inset also a red shift in the peak position for π–polaron absorption band from around 768 nm to 796 nm was seen due to the formation of nanocomposite. The red shift of absorption bands with lesser intensities implies partial bonding of PANI–CSA with CdS nanoparticles. These verifications of the shifting of different peaks have confirmed the incorporation of CdS nanoparticles to PANI–CSA.

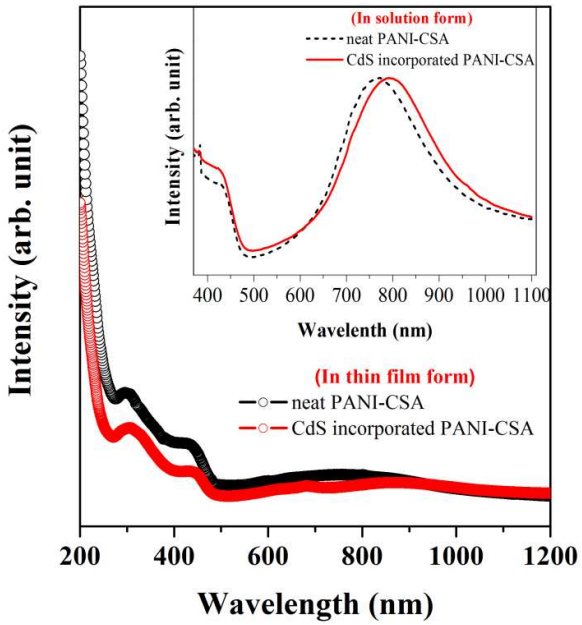

Figure 6: The UV-Visible absorption spectra of PANI–CSA and CdS incorporated PANI–CSA thin films are shown. The inset is showing the absorption spectra of the corresponding material in the solution form

3. 4. AFM Results:

3.4.1. Growth process by layer variation: The multilayer films of the CdS-PANI nanocomposite show dominating growth mechanism with the variation in height. Figure 7 shows the AFM images of 3 layers, 9 layers, 15 layers, 18 layers, 21 layers and 25 layers of CdS-PANI nanocomposite thin films within a scan size area of 10×10 μm^2.

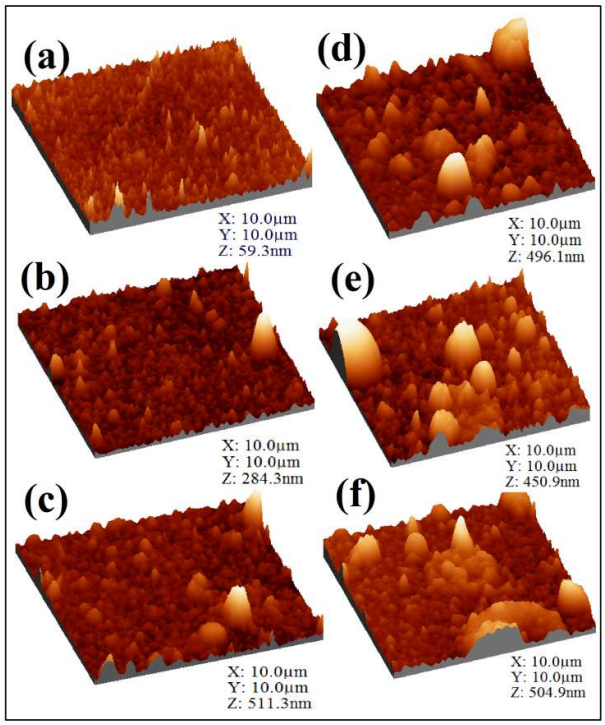

Figure 7: AFM images of CdS incorporated PANI–CSA thin films of different layers viz (a) 3 layers, (b) 9 layers, (c) 15 layers, (d) 19 layers, (e) 21 layers and (f) 25 layers.

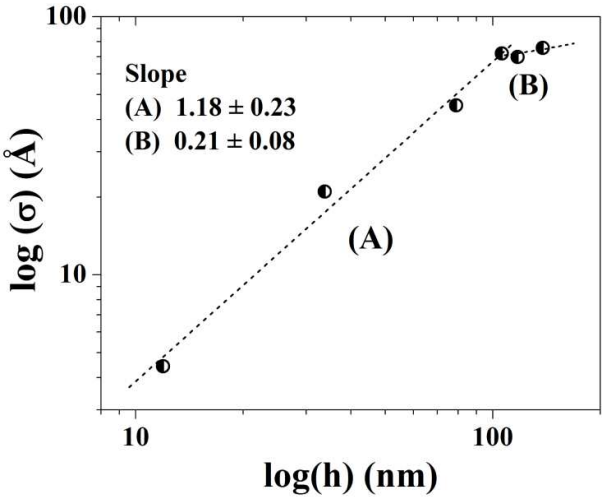

Figure 8: logarithmic variations of roughness (σ) vs. that of thicknesses (h) of different LB prepared layers are shown. The variation of roughness is shown as solid black spheres (●) and is fitted with black dash lines (---).

The growth mechanism is demonstrated as the height variation correlation over the surfaces which is measured as, $\sigma = \left\langle \left[z(x,y) - \langle z \rangle \right]^2 \right\rangle^{1/2}$ where, z(x, y) is the height at point (x, y) with

respect to mean height $\langle z \rangle$ [38]. The variation of the surface roughness with average height of the layer is shown in Figure 8. The layer variation enhances the surface roughness and within the asymptotical limit, it satisfies eq. 2. It is seen that the enhanced roughness saturates at some crossover height which gives two distinct regions of the growth. The crossover height is calculated to be h_c = 104.3 nm, which nearly agrees with earlier reported results [39]. The log-log plot between the RMS roughness and the thickness gives the growth exponents as β = 1.18±0.23 and 0.21±0.08 from linear fitting (black dash line Figure 8), showing the two separate regions of growth. The larger value of β at the initial stage of the nanocomposite mainly specifies the rapid roughening of the surfaces which arises due to the upright and tilted growth of columnar structures. The measured large growth exponents are also reported for other organic thin films e.g. free-base pthalocyanine (β=1.02±0.08) [40] and diindenoperylene (DIP) thin films on SiO_2 (β = 0.748) [41]. The other value of β as calculated points to the saturation of the roughness above the crossover height, h_c.

The change in the growth exponent at a critical film thickness may be due to following reasons. Thin films have free energy associated with them as a consequence of interactions between the substrate and air mediated by the film. This interaction can be destabilising (corresponds to a positive Hamaker constant A, which depends on the relative interactions [42]). The driving force for the destabilisation decreases as the film becomes thicker and since surface tension opposes roughening, the critical length scale for roughening increases. Moreover as the average thickness grows with the number of layers, the lateral length scale of the roughness may saturate beneath the critical length scale for it to continue to grow as this satisfies the condition, $k_c^2 < \left\{ \left(3|A|\right)^2 / \left(h_c^4 \sigma\right) \right\}$, where σ is the surface tension and k_c is the critical wave vector (see the Appendix I). Thus, the larger the increase in critical wavelength the more will be the saturation of roughness values after a certain value of h_c. The lengthscale of the pre-existing roughness at lower number of layers acts as a template for the addition of further layers, being below the critical lengthscale for thicker films.

The aforementioned thermodynamically driven roughening process also considers the kinetics of the diffusion phenomenon to grow in layers. At the initial stage, the impingement of new material is more likely to be on the protrusions or hills which carry the increment in roughness nearer to the h_c. Beyond h_c, the roughness becomes saturated as the incoming adatoms find the valleys or the grooves. The continuous deposition of new molecular layer

causes induced downhill flow of adatoms in the presence of top layer as proposed by Moseler et al. [43]. This sort of surface diffusion occurring at the top overcomes the noise induced roughening in order to saturate the same. The formation of completely smooth surface is a challenge since surface diffusion does not provide enough lateral extension resulting in certain accumulation at definite sites only (Figure 7(e) and (f)) and the rest part still adhere to the uphill accumulation of the adatoms.

3.4.2. PSD roughness evaluation: The RMS surface roughness complies with the information of vertical film growth only and it gives only the root mean square height of a surface around its mean value. However a more complete description of the surface topography is provided by the PSD of the surface roughness, which measures the lateral as well as the longitudinal variation. Such measurements perform a decomposition of the surface profile into its spatial wavelengths. The PSD of an image is usually calculated from the 2D Fourier Transform of a topographic image by angle averaging the Fourier transform in all directions.

For a surface described by z (x, y), the 2-D PSD is computed by [44],

$$S_2(f_x, f_y) \approx \frac{L^2}{N^2}\left|\sum_{n=0}^{N}\sum_{m=0}^{N} z(x_m, y_n)\exp\left(2\pi i m \frac{\Delta x}{N} f_x\right)\exp\left(2\pi i n \frac{\Delta y}{N} f_y\right)\right|^2 \qquad (4)$$

where f_x, f_y are the spatial frequencies for x and y directions, respectively and the scan length L and pixels number N are assumed to be equal in x and y directions. The 2-D PSD function contains information over the range of spatial frequencies: $f_x, f_y \in [1/L, N/(2L)]$.

In Figure 9 we show the power spectra calculated from AFM measurements against the spatial frequency. The graphs show that with gradual increase from low spatial frequency, the power spectra proceed horizontally and after certain characteristic frequency κ (region better known as white noise) the variation turns to get saturated at some higher range showing a correlation with the roughness behavior. The images acquired at different thicknesses show different slopes in correlated linear portion of the PSD spectra. The slope thus calculated from the linear portion gives the value of γ [eq. 5]. The roughness exponent (α) and its variation with the layer numbers can be calculated by using the relation [26]

$$PSD(f \rangle \xi^{-1}) = \frac{K}{f^{\gamma}} \qquad (5)$$

and for,

$$\gamma \geq d'$$
$$\alpha = \frac{\gamma - d'}{2} \quad (6)$$

Where K is the proportionality constant, d′ is the dimension of the cross-section and γ represents a constant for PSD measurements. We can also calculate the fractal dimension (D_f) of the individual surfaces by using the following equation [45],

$$D_f = \frac{8 - \gamma}{2} \quad (7)$$

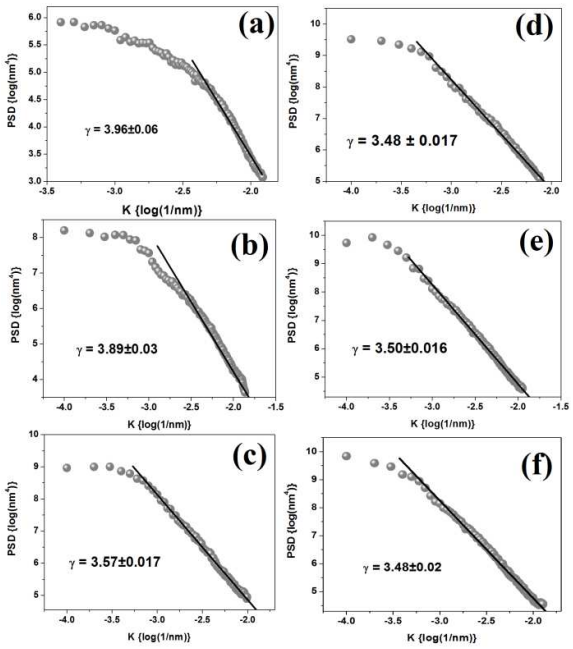

Figure 9: PSD spectrum of CdS incorporated PANI–CSA thin films of different layers viz (a) 3 layers, (b) 9 layers, (c) 15 layers, (d) 19 layers, (e) 21 layers and (f) 25 layers are shown. The linear fitting curve over the correlated portion gives value of γ.

The different parameters calculated with the help of the above details are shown in table 2. The results show that with the increase of thickness, the slopes calculated from the PSD spectra show gradual decrease. Accordingly, the roughness exponents (α) also show a decrease in their values. This suggests that with the increase of the layer thickness, the surface morphology of LB prepared CdS–PANI–CSA nanocomposite becomes more corrugated and jagged in nature. The complex behaviors of the films are also ascertained from measured fractal dimension (D_f) values which show an increase from 2.02±0.06 to 2.26±0.02 with the increase in layer thickness. From the table 2, it is seen that towards the higher thickness the

variation of D_f is almost saturated which is showing a correlation with the growth curve (Figure 8). Moreover from the Figure 9, we can see that the curves become steeper with increase in the thickness of the films which suggests a decrease of self-affine properties.

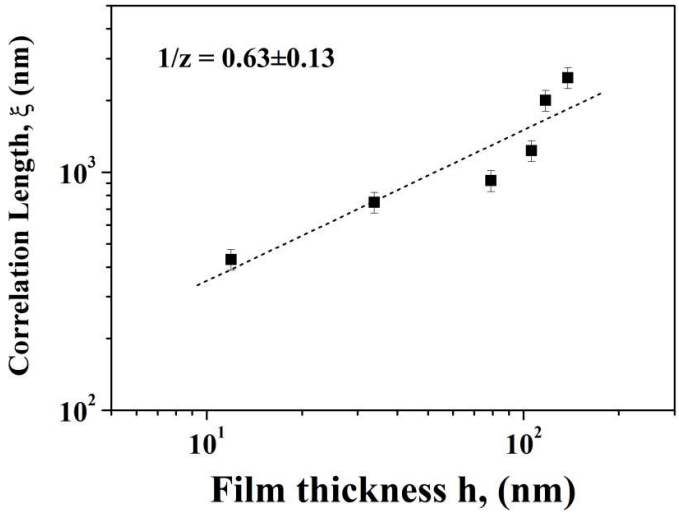

Figure 10: The logarithmic variation of the correlation length (ξ) with that of the thickness (h) for the AFM images are shown and the linear fitting calculates the coarsening factor (1/z).

In Figure 9, the plateau of linear variation in the PSD spectra indicates the roughness height of the respective AFM images. Since the roughness saturates at certain length scale, a characteristic correlation length (ξ) of each layer can be evaluated from the power spectra by spotting the spatial frequency, where PSD falls to *1/e* of its saturation low frequency value [26]. The dynamic scaling factor (z) can be calculated from the variation of ξ values with respect to h which is given by the power law, $\xi = bh^{1/z}$ [26], where b is the proportionality constant. Figure 10 shows such a log-log variation of ξ and h from which the value of $1/z = 0.63 \pm 0.13$ has been calculated; the quantity, 1/z is called the coarsening exponent [39]. The coarsening exponent can also be calculated from correlation between the exponents α, β and z by using the scaling law, $1/z = \beta/\alpha$. Using the values of α and β (from our calculations) the value 1/z is found to be 1.42±0.07. The two different values of 1/z as calculated from two different approaches signify a fault in the assumption of the origin of the roughness length. Such inequality in 1/z value is also reported in case of the other organic thin films [40]. It has been concluded that for long (global) and short (local) length scale the characteristic growth and roughness exponents shows substantial fluctuation and that can be correlated to some modified scaling law. The modified scaling law which shows the deviation in self-affine scaling ansatz is given as [22, 40, 46],

$$\beta = \alpha_{loc} / z + \lambda \quad (8)$$

Where, λ is the steepening constant and for λ = 0, the surface is truly self-affine.

From the results, the interface width is found to be no longer time dependent at short length scale hence it follows a power law with a new exponent β_{loc}, while at large scales it scales as h^{β}. Now, one can preferably write the relations $\alpha_{loc} = \alpha - \beta_{loc} z$ and $\alpha_{loc} = (\beta - \beta_{loc}) z$. Relating the non-unique behavior of the dynamic scaling factor to the global and the local variation of the growth exponent (β) we can calculate the steepening constant (λ) to be ~0.66 by using eq. 8. The value of 0.66 is found to be significantly larger than the condition for self-affine behavior which is due to pronounced "intrinsic" anomalous scaling effect as suggested by Ramasco et al. [47].

3.4.3. Surface morphology of CdS-PANI thin films with layer variation:

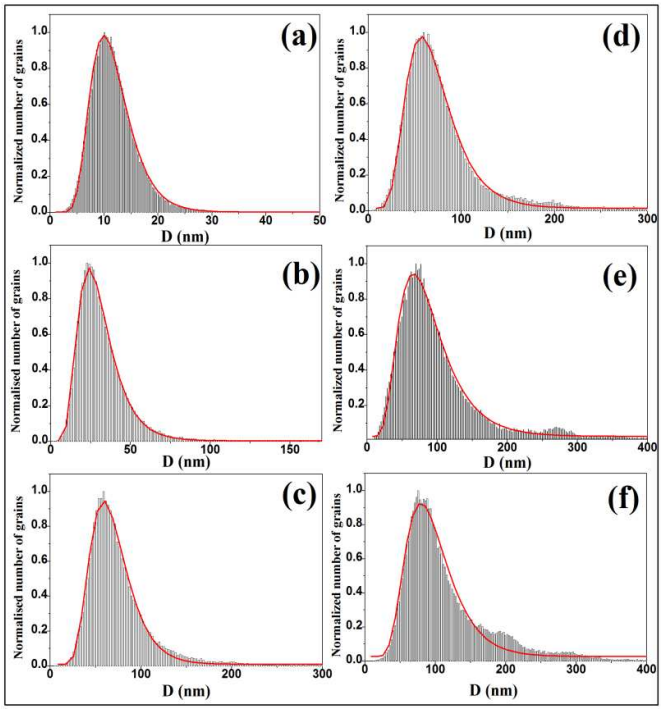

Figure 11: Distribution and aggregation of CdS incorporated PANI–CSA nanocomposite are shown as the histograms for the different layers viz. (a) 3 layers, (b) 9 layers, (c) 15 layers, (d) 19 layers, (e) 21 layers and (f) 25 layers. The distribution graphs are the evidence of monomodal and the bimodal distribution of the nanocomposites over the surfaces. The red curve suggests the lognormal fitting of the distribution from which the average size of the distributed particle is calculated.

The surface roughness is clearly understood when proper distribution of grains over the surface is examined for CdS–PANI–CSA nanocomposites. The AFM images show that as thickness of film increases, some grains have grown in sizes and have accumulated over the

surfaces (Figure 7). The grain growth and the distribution of the grains on the film surfaces are shown as histograms in Figure 11. The histograms are drawn as the normalized grain counts with respect to the variation of the grain sizes of the films. Formation of the normal and abnormal grains can be distinguished from the histogram by monomodal distributions as shown in Figure 11(a–c) and the bimodal distribution in Figure 11(d–f) respectively [48, 49]. For the quantitative analysis of the normal grain size distribution, the envelops of the histograms are fitted by the log-normal function,

$$y = \frac{A}{\sqrt{2\pi}\sigma D}\exp\left[-\left(\frac{\ln^2(D/D_c)}{2\sigma^2}\right)\right] \quad (9)$$

Where, D is the grain diameter in each sample and σ is the standard deviation on D. A is the proportionality constant. The fitting parameters are tabulated in table 3. The quantitative results show the variation of the grain sizes from 11.2 nm to 91.5 nm with the increase in layer numbers. In Figure 11(d–f) the normal grain distribution is accompanied by small humps, showing the presence of abnormal grain formation.

Grain boundary anisotropy and the difference in surface free energy may lead to the abnormal grain formation. It is found that initially, the grain growth depends on the interaction between the substrate and the first deposited film layer which corresponds to a constant chemical potential [50]. As the number of deposition increases the parameters such as the grain boundary anisotropy, strain, compositional variation, motion of grains etc. overcome the interfacial chemical potential and thus lead to the spherical or columnar grain growth over the surfaces [51]. The grains with average sizes will grow continuously and as a result the distribution becomes monomodal. Later on, some of the grains grow at higher rate as compared to the normally growing grains and they may get annihilated to form the abnormal grains.

3.4.4. Grain growth over film surfaces and grain agglomeration: Thin films of PANI doped with CSA have shown some uniform cylindrical/globular shaped nano-grain structure (Figure 12(a)). The globular phase of the nanoparticles is formed due to the lateral and vertical nucleation of polymer molecules while doping with CSA. The protonation of high-polarity sulphonic acid group to the imine group of the polymer structure may lead to the formation of hydrophilic and hydrophobic planes within the polymer chain [52]. The bending of such specific planes during compression over the LB trough may solubilize the aromatic rings of the polymer molecule to form spherical shapes.

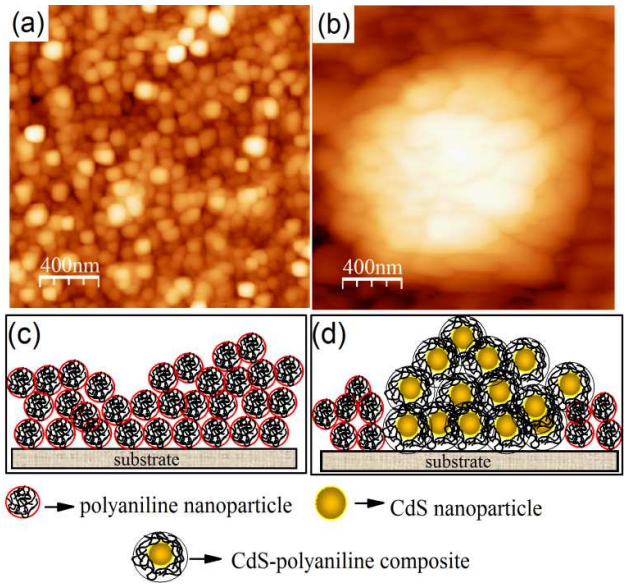

Figure 12: (a) The globular shaped PANI-CSA thin film before CdS incorporation (b) A specific portion of agglomeration of CdS incorporated PANI-CSA thin film. The image scan size is compared within 2 × 2 μm^2 scan area. (c) and (d) show a tentative schematic diagram of formation of neat PANI-CSA and CdS-PANI-CSA composite.

When CdS nanoparticles are incorporated with the globular shaped PANI–CSA nanocomposites, they are absorbed and diffused laterally through the polymer chains. The diffusion may cause the agglomeration of the nanocomposites. Figure 12(b) is showing such an agglomerated section of the composite thin film surface. A tentative schematic diagram of the formation of the composite before and after the incorporation of the CdS nanoparticle has been shown in Figure 12(c-d). The absorption of the CdS nanoparticles in polymer matrix can take place easily due to the weak bonding between the polymer chains [53]. Increasing the number of layers enhances the incorporation of the adatoms to the previously settled atoms or in the vacancies over the surfaces, thereby promoting the formation of the stable nucleated particle. With time and with the increase of the number of layers the nucleated particles grow in size [table 3]. The growth phenomenon of the nucleated particles can be explained by the process of "Ostwald ripening" [54]. The nucleation with deposition continues until a state is reached where the probability of diffusion of the adatoms to join the existing cluster dominates over the formation of some new nucleated particles. Thus the cluster formation increases because of the lateral growth of the particles via diffusion process [Figure 12(b)]. The diffusion driven coalescence of the cluster is termed as the "Smoluchowski ripening" [55]. In Figure 8, the saturated part in the growth curve confirms diffusion driven coalescence of the clusters.

3.5. X-ray Reflectivity (XRR) studies:

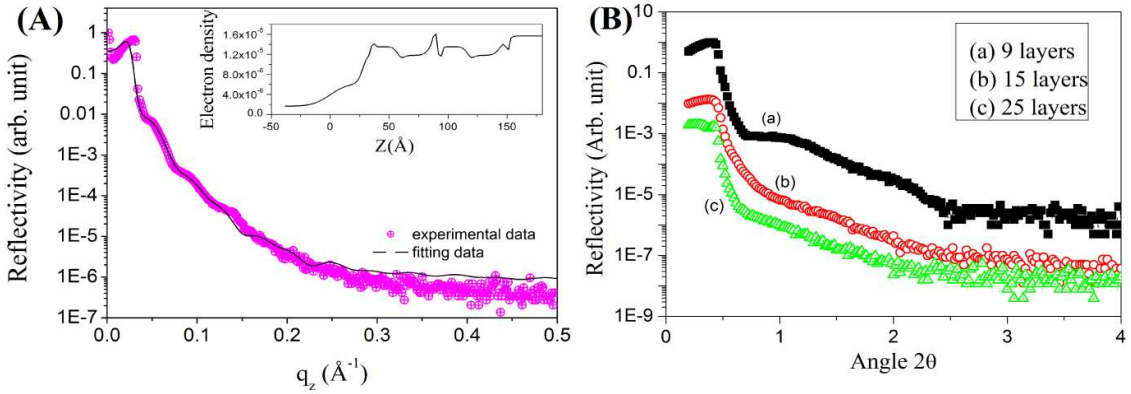

Figure 13: (A) XRR patterns and the fitting of 3 layers of CdS incorporated PANI-CSA thin films; in the inset the electron density profile of the same is presented (B) XRR spectra of (a) 9 layers, (b) 15 layers and (c) 25 layers.

The layer-by-layer variation of CdS incorporated PANI–CSA composites are confirmed by the XRR measurements [56] as shown in Figure 13. In Figure 13(A), reflectivity pattern of 3 layer of the nanocomposite film is shown and fitted with parratt32 software; XRR patterns of another 9 layer, 15 layers and 25 layers with angle variation are shown in Figure 13(B). From Figure 13(A), it can be concluded that for a small number of layer stack head-to-head/tail-to-tail deposition of the amphiphilic polymer nanocomposite is possible and diffusion takes place while increasing the numbers of layers due to either electrostatic interaction or formation of H-bonding [7, 57]. With the best of fitting for the 3 layers of CdS-PANI, the thickness of the film is calculated to be ~13.4 nm which is close to the value calculated from the AFM measurements. The electron density within the bilayer as calculated from fitting varies from 1.43×10^{-5} (Å)$^{-2}$ (top layer) to 6.19×10^{-6} (Å)$^{-2}$ (bottom layer). The sharp dips of electron density profile (1.99×10^{-5} (Å)$^{-2}$) refers to highly electron dense site as shown in inset of Figure 13(A) which may be due to the presence of the CdS nanoparticles. The roughness that came out from the fitting for 3 layers of CdS incorporated PANI-CSA thin films is found to be 3.95 nm. This value is lesser than that from AFM measurements and within the error range such deviation may be assigned to the limitation of the AFM instrument. Further increasing the number of layers, the reflectivity patterns show some highly diffusing structures and also the prominent Kiessig fringes are found to be vanished [Figure 13(B)]. Such reflectivity patterns indicate the formation of irregular films with increased roughness.

Either the electrostatic interaction between CdS nanoparticles and PANI or the H-bonding in PANI may cause the diffusion of layers thereby increasing the interfacial roughness.

4. Conclusions:

In this article, the kinetic roughening and the growth mechanisms of CdS nanoparticle induced PANI-CSA thin films synthesized by LB technique are studied. We used different characterization techniques such as XPS, HRTEM, AFM and XRR to study these films. Taking growth kinetics and dynamic scaling properties of the surfaces with layer variation as the prime attention of discussion the following conclusions are made:

Formation of the CdS nanoparticles within the dimension of 6-9 nm is confirmed by the HRTEM results. Layer variation synthesis of the CdS-PANI-CSA nanocomposites by LB technique have shown a large value of growth exponent β (=1.18±0.03) which points to the rapid roughening of surfaces during the growth of layers. The roughness exponent (α) as calculated from the PSD measurements is also found to be 0.82±0.04. With the help of a definite scaling relation between the different exponents the coarsening factor $1/z = 1.42\pm0.07$ has been calculated. The value of $1/z = 0.63\pm0.13$ is also evaluated from the log-log variation between the correlation length and height of films. It is observed that using the classical scaling law we do not obtain the same result for dynamic scaling factor and hence a modified scaling law with a steepening constant (λ) has been applied which explains the difference in the global and the local growth exponent values. A large value of λ in our calculation signifies a deviation from the self-affine condition which arises due to the anomalous roughening during the film growth.

The roughness anomaly over the surfaces is also demonstrated by abnormal and normal grain growth mechanism. In our study the normal grain growth is found to have a monomodal log-normal distribution whereas the abnormal grain growth is explained by the bimodal distribution.

Results of AFM studies are correlated to the results of XRR which agrees more for the smaller number (3 layer) of depositions. On the other hand by increasing layer number, the XRR spectra are found to be highly diffusing in nature due to electrostatic interaction or the formation of H-bonding.

We believe that the present study of the film growth will help in making better surface enhanced CdS-PANI thin films for optoelectronic application.

Acknowledgement:

We would like to thank Dr. M. Gupta of UGC-DAE CSR, Indore for useful discussions. We also like to acknowledge Dr. V. Reddy of UGC-DAE CSR Indore for the XRR measurements and Dr. T. Shripathi, UGC-DAE CSR Indore for the XPS measurements. We thank Dr. N. Shakti, IIT Delhi for the HRTEM measurements of our samples. The financial assistance from UGC-DAE CSR Indore under the CRS project scheme is also acknowledged. Two of the authors also like to thank UGC, India for the financial assistance.

Appendix-1

A thermodynamic explanation can be given for the roughness saturation as the average thickness increases. The local free energy of thin film is given by the relation,

$$F = -\frac{A}{h^2} + \sigma\left(\Delta h\right)^2$$

Where h is the local height and A is Hamaker constant and σ is the surface tension

When A> 0, the film is unstable to height fluctuations that are greater than a critical lateral lengthscale. Consider a film in 1D with profile

$$h = h_c + \delta h \sin(kx)$$

Where, k is the wave vector

Therefore we have,

$$f \approx -\frac{A}{h_c^2} + \left(\frac{3A\sin^2(kx)}{h_c^4} + h^2\sigma\cos^2(kx)\right)\delta h^2$$

Now, the total free energy over one complete wavelength of fluctuation will be

$$\begin{aligned} F &= \int_0^{2\pi/k} f\left(x\right)dx \\ &= \pi\left[-\frac{8A}{4h_c^2k} + \left(\frac{3A}{h_c^2} + \sigma k\right)\delta h^2\right] + \text{higher order terms} \\ &= F\left(h_c\right) + \left(-\frac{3A}{h_c^2} + \sigma k\right)\delta h^2 + \text{higher order terms} \end{aligned}$$

Thus a film can lower its surface free energy by roughening if A>0, and

$$\left(-\frac{3A}{h_c^2} + \sigma k_c \right) < 0$$

$$k_c^2 < \frac{\left(3|A|\right)^2}{h_c^4 \sigma}$$

Hence, as h_c increases the critical wave vector for fluctuation decreases which correspond to an increase in wavelength.

References:

1. M. Grätzel, *Nature*, 2001, **414,** 338.

2. N. C. Greenham, X. Peng and A. P. Alivisatos, *Phys. Rev. B*, 1996-II, **54**(Dec 15), 17628.

3. B. J. Gallon, R. W. Kojima, R. B. Kaner and P. L. Diaconescu, *Angew. Chem. Int. Ed.,* 2007, **46**(38), 7251

4. D. W. Hatchett and M. Josowicz *Chem. Rev.,* 2008, **108,** 746.

5. M. A. Rahman, J. I. Son, M.-S. Won and Y.-B. Shim, *Anal. Chem.,* 2009, **81,** 6604

6. E. W. H. Jager, E. Smela and O. Inganäs, *Science,* 2000, **290,** 1540

7. J. H. Cheung, W. B. Stockton and M. F. Rubner, *Macromolecules,* 1997, **30,** 2712.

8. N. M. Das, D. Roy and P. S. Gupta, *Mater. Res. Bull.,* 2013, **48,** 4223

9. R. Shenhar, T. B. Norsten and V. M. Rotello, *Adv. Mater.,* 2005, **17**(6), 657

10. P. Akcora, H. Liu, S. K. Kumar, J. Moll, Y. Li, B. C. Benicewicz, S. L. Schadler, D. Acehan, A. Z. Panagiotopoulos, V. Pryamitsyn, V. Ganesan, J. Ilavsky, P. Thiyagarajan, R. H. Colby and J. F. Douglas, *Nat. Mater.,* 2009, **8,** 354.

11. Y.-F. Lin, C.-H. Chen, W.-J. Xie, S.-H. Yang, C.-S. Hsu, M.-T. Lin and W.-B. Jian, *ACS Nano*, 2011, **5**(2), 1541.

12. C. Zhou, J. Han and R. Guo, *Macromolecules,* 2009, **42,** 1252

13. L. H. Huo, L. X. Cao, D. M. Wang, H. N. Cui, G. F. Zeng and S. Q. Xi, *Thin Solid Films,* 1999, **350,** 5.

14. J. Zhang, D. P. Burt, A. L. Whitworth, D. Mandler, and P. R. Unwin, *Phys. Chem. Chem. Phys.,* 2009, **11,** 3490.

15. K. Dutta, S. De and S. K. De, *J. Appl. Phys.,* 2007, **101,** 093711

16. D. Y. Godovsky, A. E. Varfolomeev, D. F. Zaretsky, R. L. N. Chandrakanthi, A. Kündig, C. Weder and W. Caseri, *J. Mater. Chem.*, 2001, **11,** 2465.

17. N. P. Gaponik and D. V. Sviridov, *Ber. Bunsen-Ges. Phys. Chem.,* 1997, **101,** 1657.

18. N. C. Greenham, X. Peng and A. P. Alivisatos, *Phys. Rev. B* 1996, **54(24)** 17628

19. N. C. de Souza, M. Ferreira, K. Wohnrath, J. R. Silva, O. N. Jr. Oliveira and J. A. Giacometti, *Nanotechnology,* 2007, **18,** 075713.

20. P. Olejnik, M. Gniadek and B. Palys, *J. Phys. Chem. C*, 2012, **116,** 10424.

21. M. Ferreira, K. Wohnrath, R. M. Torresi, C. J. L. Constantino, R. F. Aroca, O. N. Jr. Oliveira and J. A. Giacometti, *Langmuir*, 2002, **18,** 540.

22. J. Santamaria, M. E. Gomez, J. L. Vicent, K. M. Krishnan and I. K. Schuller, *Phys. Rev. Lett*., 2002, **89 (19),** 190601

23. A. L. Barabási and H. E. Stanley, *Fractal Concepts in Surface Growth* (Cambridge University Press, New York, 1995)

24. J. F. G. Martínez, I. N. Carvajal, J. Abad and J. Colchero, *Nanoscale Res. Lett*., 2012, 7, 174.

25. K.A. Takeuchi, M. Sano, T. Sasamoto and H. Spohn, *Sci. Rep*., 2011, **1, 34,** 1–5, DOI: 10.1038/srep00034.

26. F. Ruffino, M. G. Grimaldi, F. Giannazzo, F. Roccaforte and V. Raineri, *Nanoscale Res. Lett*., 2009, **4,** 262

27. I. Horcas, R. Fernandez, J. M. G. Rodríguez, J. Colchero, J. G. Herrero and A. M. Baro, *Rev. Sci. Instrum.,* 2007, **78,** 013705.

28. S. Ameen, M. S. Akhtar, M. Song and H. S. Shin, Metal Oxide Nanomaterials, Conducting Polymers and Their Nanocomposites for Solar Energy**.** In *Solar Cells-Research and Application Perspectives,* ISBN 978-953-51-1003-3; Morales-Acevedo, A.; InTech: Janeza Trdine 9, 51000 Rijeka, Croatia, **2013**; 203-259

29. J. D. G. Durán, M. C. Guindo, A. V. Delgado and F. G. Caballero, *J. Colloid Interface Sci.,* 1997, 193, 223.

30. H. Wang and S. Mu, *Sens. Actuators B: Chem.,* 1999, **56,** 22.

31. D. Roy, N. M. Das and P. S. Gupta, *Appl. Surf. Sci*., 2013, **271,** 394.

32. R.L.N. Chandrakanthi, M.A. Careem, *Thin Solid Films* 2002, **417**, 51

33. J. Park, D. Bang, K. Jang, S. Haam, J. Yang, S. Na, *Nanotechnology,* 2012, **23**, 365705

34. S. Singh, R. S. Deol, M.L. Singla, D.V.S. Jain, *Sol. Energ. Mat. Sol. C.,* 20014, **128,** 231

35. V. R. Mehto, D. Rathore, R.K. Pandey, (2014), doi: 10.1002/pc.22842

36. P.S. Khiew, N.M. Huang, S. Radiman, Md. S. Ahmad, *Mater. Lett.,* 2004, **58,** 516.

37. P.K. Khanna a, S. P. Lonkar, V.V.V.S. Subbarao, K.-W. Jun, *Mater. Chem. Phys.* 2004, **87,** 49

38. J. K. Bal and S. Kundu, *J. Appl. Phys*. 2013, **113,** 114905.

39. M. E. Vela, G. Andreasen, R. C. Salvarezza, A. J. Arvia, *J. Chem. Soc.,Faraday Trans.,* 1996, **92(20)** 4093.

40. S. Yim and T. S. Jones, *Phys. Rev. B*, 2006, **73,** 161305(R)

41. A. C. Dürr, F. Schreiber, K. A. Ritley, V. Kruppa, J. Krug, H. Dosch and B. Struth, *Phys. Rev. Lett.*, 2003, **90**(1), 016104.

42. J. N. Israelachvili, *Intermolecular and Surface Forces*. (Academic Press, Burlington, MA 01803, USA, third edition 2011; ISBN: 978-0-12-375182-9)

43. M. Moseler, P. Gumbsch, C. Casiraghi, A. C. Ferrari and J. Robertson *Science, 2005,* **309,** 1545

44. R. Gavrila, A. Dinescu, D. Mardare, *International semiconductor conference*, Sinaia, 2006, ISBN: 1-4244-0109-7, pg. no. 167–170, DOI: 10.1109/SMICND.2006.283959

45. D. Raoufi, *Physica B*, 2010, **405,** 451.

46. J. Soriano, J. J. Ramasco, M. A. Rodríguez, A. H, Machado and J. Ortín, *Phys. Rev. Lett.,* 2002, **89**(2), 026102.

47. J. J. Ramasco, J. M. Lopez and M. A. Rodriguez, *Phys. Rev. Lett.*, 2000, **84,** 2199

48. C. V. Thompson, *J. Appl. Phys*., 1985, **58,** 763.

49. F. Ruffino, M. G. Grimaldi, C. Bongiorno, F. Giannazzo, F. Roccaforte, V. Raineri, C. Spinella, *J. Appl. Phys.,* 2009, **105** 054311.

50. P. Liu, C. Lu and Y. W. Zhang, *Phys. Rev. B*, 2007, **76,** 085336.

51. M. Bouville, *Appl. Phys. Lett.* 2007, **90**, 061904

52. H. D. Tran, J. M. D'Arcy, Y. Wang, P. J. Beltramo, V. A. Strong, R.B. Kaner, J. Mater. Chem., 2011, 21, 3534

53. L. H. Cai, S. Panyukov, M. Rubinstein, *macromolecules* 2011, **44,** 7853.

54. D. Y. Protasov, W. B. Jian, K. A. Svit, T. A. Duda, S. A. Teys, A. S. Kozhuhov, L. L. Sveshnikova and K. S. Zhuravlev, *J. Phys. Chem. C*, 2011, **115,** 20148.

55. G. Kaune, M. A. Ruderer, E. Metwalli, W. Wang, S. Couet, K. Schlage, R. Röhlsberger, S. V. Roth and P. M. Buschbaum, *ACS Appl. Mater. Interfaces*, 2009, **1**(2), 353.

56. T. P. Russell, *Mater. Sci. Rep.,* 1990, **5,** 171.

57. W. B. Stockton and M. F. Rubner, *Macromolecules*, 1997, **30,** 2717

Table 1: *FTIR spectra showing the different bands of neat PANI-CSA and CdS incorporated PANI-CSA nanocomposites*

Wave number (cm^{-1}) (solution) Neat PANI-CSA	Wave number (cm^{-1}) (solution) CdS-PANI-CSA composite	Wave number (cm^{-1}) (thin film) CdS-PANI-CSA composite	Band characteristics
615.30	612.47	608.67	C–H out of plane bending vibration
774.06	777.58	752.96	Paradisubstituted aromatic rings indicating polymer formation
1047.12	1047.12	1050.49	Due to SO^{-3}group of the CSA
1167.07	1165.68	1167.78	vibration mode of N=Q=N [32]
1383.69	1383.24	1330.05	Aromatic C–N stretching indicating a secondary aromatic amine group
1459.15	1462.38	1457.79	C=C and C=N stretching of benzenoid rings [33]
1592.54	1592.54	1578.3	C=C and C=N stretching of quinoid rings
1737.89	1737.89	--------	May be due to stretching of C=N-bond [34]

Table 1*: Calculation of roughness exponent (α) and fractal dimension (D_f) from the slope (γ) of the power spectra*.

No. of Layers	γ	Roughness exponent, α	Avg. of roughness exponent, α	Fractal Dimension, D_f
3	3.96±0.06	0.98±0.03		2.02±0.03
9	3.88±0.03	0.94±0.02		2.06±0.02
15	3.57±0.02	0.79±0.01	0.82±0.04	2.22±0.01
18	3.48±0.02	0.74±0.01		2.26±0.01
21	3.50±0.01	0.75±0.01		2.25±0.01
25	3.48±0.02	0.74±0.01		2.26±0.01

Table 2*: lognormal fitting parameters for the different layers*

layers	Avg. ht. (nm)	Constant, A	Standard deviation, σ	D_c (nm)
3	11.9	8.74± 0.03	0.34 ±0.02	11.15 ±0.02
9	33.8	26.12 ±0.07	0.41 ±0.02	28.38 ±0.04
15	79.1	49.45± 0.24	0.33 ±0.01	65.78 ±0.13
19	106.1	59.29 ±0.32	0.39 ±0.01	66.70 ±0.18
21	117.4	76.90 ±0.51	0.45 ±0.04	81.23 ±0.32
25	137.9	71.90± 0.78	0.37± 0.08	91.45 ±0.46